Freely Tunable Broadband Polarization Rotator for Terahertz Waves

Ren-Hao Fan, Yu Zhou, Xiao-Ping Ren, Ru-Wen Peng, Shang-Chi Jiang, Di-Hu Xu, Xiang Xiong, Xian-Rong Huang,* and Mu Wang**

Terahertz (THz) waves, which possess wavelengths between infrared light and microwaves in the electromagnetic spectrum, have been intensively studied in recent years due to the emergence of efficient THz sources and sensitive detectors.[1–3] Nowadays, the THz technology has a variety of unprecedented applications in information and communications technologies, advanced imaging, bio- and medical sciences, homeland security, etc. Yet further development of THz materials/devices in the frequency range of 10^{11}–10^{13} Hz has been restricted mainly due to the lack of tunable, high-efficiency, and broadband optical components including polarization converters and rotators,[4–18] phase modulators,[19–21] and lenses.[22,23] It is known that commercially available THz emitters usually generate linearly polarized waves only along certain directions, but in practice, a polarization rotator that is capable of rotating the polarization of THz waves to any direction is particularly desirable and it will have various important applications.

Conventionally, the polarization direction of a linearly polarized THz wave is modulated by birefringent crystals[24,25] or liquid crystals.[26–28] However, the available materials can only be applied to a very narrow frequency band of THz waves. Very recently, by introducing THz metamaterials researchers are able to change the polarization of broadband THz waves.[13,14] Specifically, the metamaterial-based broadband THz polarization converter has been proposed and demonstrated to have a powerful capability of rotating a linear polarization state into its orthogonal state.[13] Tri-layer metasurfaces can also efficiently rotate the linear polarization of THz waves in a broadband range.[14] Despite of these achievements, however, a common limitation of such devices is that each metastructure can tune the polarization only to a specific direction based on its design, i.e., these rotators cannot freely rotate the polarization to arbitrary directions.

In this communication, we demonstrate for the first time a freely tunable polarization rotator for broadband THz waves using a three-rotating-layer metallic grating structure, which can conveniently rotate the polarization of a linearly polarized THz wave to any desired direction with nearly perfect conversion efficiency. It is a subwavelength device that has a thickness less than one quarter of the central wavelength in the working frequency band. The device performance has been experimentally demonstrated by both THz transmission spectra and direct

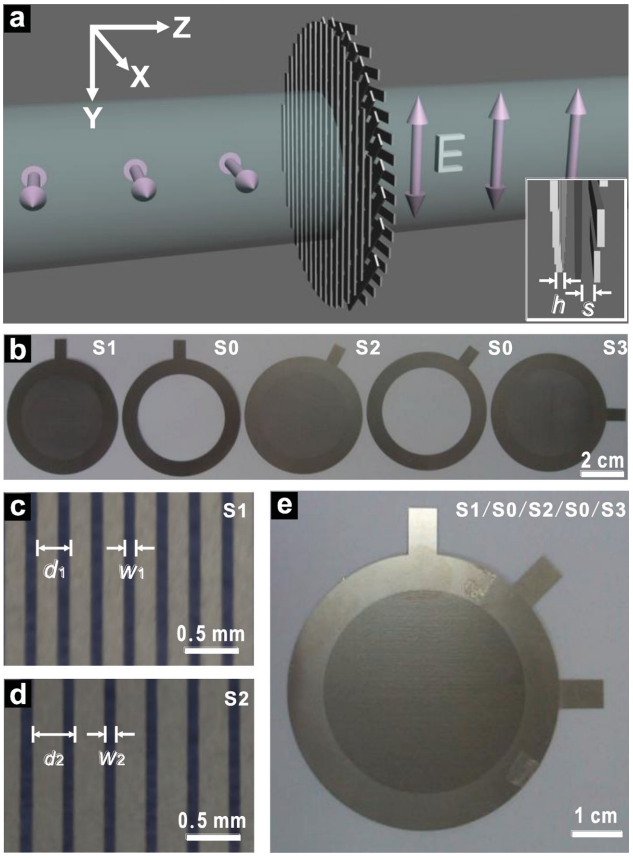

Figure 1. Construction of the freely tunable broadband linear polarization rotator for THz waves. a) Schematic of the three-grating-layer rotator. The inset represents part of the lateral view. b) Photographs of the five components of the polarization rotator. c) Magnified photograph of S1. d) Magnified photograph of S2. e) Assembled polarization rotator with $\phi_1 = \phi_2 = 45°$.

Dr. R.-H. Fan, Dr. Y. Zhou, Mr. X.-P. Ren,
Prof. R.-W. Peng, Dr. S.-C. Jiang, Dr. D.-H. Xu,
Dr. X. Xiong, Prof. M. Wang
National Laboratory of Solid State Microstructures
and School of Physics
Collaborative Innovation Center
of Advanced Microstructures
Nanjing University
Nanjing 210093, China
E-mail: rwpeng@nju.edu.cn; muwang@nju.edu.cn
Dr. X.-R. Huang
Advanced Photon Source
Argonne National Laboratory
Argonne, Illinois 60439, USA
E-mail: xiahuang@aps.anl.gov

DOI: 10.1002/adma.201404981

imaging. The polarization rotation originates from multi wave interference in the three-layer grating structure based on the scattering-matrix analysis. We can expect that this active broadband polarization rotator has wide applications in analytical chemistry, biology, communication technology, imaging, etc.

As shown in **Figure 1**a, our freely tunable broadband linear polarization rotator consists of three layers of metallic gratings with the same thickness h. The first and second gratings have periods d_1 and d_2, and slit widths w_1 and w_2, respectively; while the third grating has the same parameters as the first one. The thickness of the air space between the neighboring grating layers is s. All three gratings can be freely rotated, and we define the rotation angle between the first and second gratings as ϕ_1, and that between the second and third gratings as ϕ_2. Figure 1b shows the five components we used to construct the polarization rotators. Here, S1 (magnified in Figure 1c) is a stainless steel grating with period d_1 = 300 μm, slit width w_1 = 120 μm, and thickness h = 50 μm; the stainless steel grating S2 (magnified in Figure 1d) has the parameters d_2 = 380 μm, w_2 = 120 μm, and h = 50 μm; S3 is the same grating as S1; and S0 is a 50-μm-thick separate layer. The assembled three-layer grating structure "S1-S0-S2-S0-S3" is shown in Figure 1e, where the thickness of the two air spacers is s = 60 (±2) μm, which is about 10 μm thicker than separate layer S0 because of the extra air gap between stainless steel layers.

The incident wave has the transverse-magnetic (TM) polarization with electric field $\mathbf{E}_0$ perpendicular to the strips of the first grating ($\mathbf{E}_0$ along the **X**-axis in Figure 1a). Numerical computations based on the finite-difference time-domain (FDTD) method[29] were also carried out with the commercially available Lumerical FDTD Solution 8.0.1 software. Because metals in the THz band can be considered as perfect electric conductors, we have set the relative permittivity of the stainless steel to –1 and the conductivity to 1.6×10^7 $(\Omega m)^{-1}$ in the calculations.

For the three-layer grating device, we define the angle

$$\Phi = \phi_1 + \phi_2 \tag{1}$$

as the designed total linear polarization rotation angle, i.e., it is anticipated that the linear polarization state of the incident beam will be rotated by angle Φ after the transmission. Our calculations show that high polarization rotation efficiency occurs at $\phi_1 = \phi_2$, so we always set $\phi_1 = \phi_2 = \phi = \Phi/2$ in this work. As mentioned above, we set the incident electric field $\mathbf{E}_0$ to be perpendicular to the strips of the first grating (TM polarization). We write the transmitted electric field as $\mathbf{E} = \mathbf{E}_{||}(\Phi) + \mathbf{E}_{\perp}(\Phi)$, where $\mathbf{E}_{||}(\Phi)$ and $\mathbf{E}_{\perp}(\Phi)$ are the components polarized parallel and perpendicular to the designed polarization direction (rotated by Φ from the X-axis to the Y-axis in Figure 1a), respectively. In order to verify the polarization rotation induced by the device, we also define two parameters $T_{||}(\Phi) = |\mathbf{E}_{||}(\Phi)|^2/|\mathbf{E}_0|^2$ and $T_{\perp}(\Phi) = |\mathbf{E}_{\perp}(\Phi)|^2/|\mathbf{E}_0|^2$, which represent the transmission components along the two orthogonal directions.

If the rotation angle between the neighboring gratings is set as ϕ = 45° in the device, we have the total polarization rotation angle $\Phi = 2\phi = 90°$. Then we expect that the input wave will be simply rotated into an orthogonally polarized output wave, i.e., $T_{||}(\Phi) \to 1$ and $T_{\perp}(\Phi) \to 0$. As shown in **Figure 2**a, our calculations indeed verify that $T_{||}(\Phi)$ reaches ~90% while $T_{\perp}(\Phi)$ is less than 1% in the frequency band 0.20–0.44 THz. It is more interesting to see that the experimentally measured $T_{||}(\Phi)$ and $T_{\perp}(\Phi)$ in Figure 2b agree well with the calculations, with $T_{||}(\Phi) \sim 90\%$ and $T_{\perp}(\Phi) < 1\%$. The polarization extinction ratio $T_{||}(\Phi)/T_{\perp}(\Phi)$ is better than 100:1 (see Figure S2 in the Supporting Information) for the shaded frequency in Figures 2a and 2b, which indicates that the output wave is a high-quality linearly polarized wave. Here, we define the polarization conversion efficiency as

$$\eta = \left|E_{||}(\Phi)\right|^2 / \left|E_0\right|^2 \equiv T_{||}(\Phi) \tag{2}$$

The results of η or $T_{||}(\Phi)$ in Figures 2a and 2b for Φ = 90°, therefore, demonstrate successful and nearly perfect polarization conversion for broadband THz waves through the three-layer metallic grating device.

Moreover, by rotating the three composite grating layers, we can freely tune the polarization rotation (Φ) of the rotator to any desired angle, which is particularly convenient for users in actual applications because additional tuning devices are not required. The calculated and experimentally measured

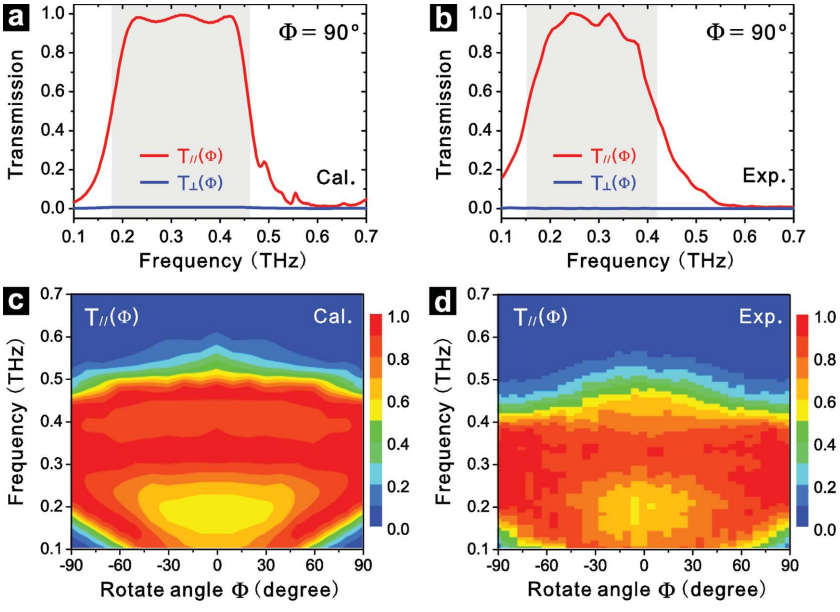

Figure 2. Measurements and calculations of the transmission of a free-tunable broadband linear polarization rotator. a) Calculated and b) measured transmission components $T_{||}(\Phi)$ and $T_{\perp}(\Phi)$ of the broadband linear polarization rotator with rotation angle Φ = 90°. The frequency regions with $T_{||}(\Phi) > 50\%$ are shaded. c) Calculated and d) measured transmission component $T_{||}(\Phi)$ (i.e., the polarization conversion efficiency η) of the polarization rotator with varying angle Φ from –90° to 90°. Color bars show intensity levels of $T_{||}(\Phi)$. The incident wave is TM-polarized with respect to the first grating S1. d_1 = 300 μm, w_1 = 120 μm, d_2 = 380 μm, w_2 = 120 μm, h = 50 μm, and s = 60 μm.

$T_{||}(\Phi)$ (i.e., polarization conversion efficiency η) of the broadband linear polarization rotator with Φ varying from –90° to 90° are shown in Figure 2c and Figure 2d. When the rotation angle ($|\Phi|$) decreases, the working bandwidth of the polarization rotator significantly increases although the polarization conversion efficiency slightly decreases. Meanwhile, due to $T_{\perp}(\Phi) < 1\%$ for all Φ varying from –90° to 90° (see Figure S3 in the Supporting Information), the $T_{||}(\Phi)/T_{\perp}(\Phi)$ is always better than 100:1 (see Figure S4 in the Supporting Information), which again indicates that the output waves are high-quality linearly polarized waves. Therefore, it is verified by the THz transmission spectra that this device can indeed work as a freely tunable broadband polarization rotator for THz waves. Besides, this polarization rotator is a subwavelength device with a total thickness of 270 μm, so it can be conveniently placed into compact optical circuits or devices for practical applications.

In order to reveal the underlying physics of the polarization rotation, we have performed theoretical analyses based on the scattering matrix method (see the Supporting Information for details).[30–32] First, we consider the polarized waves going through a metallic grating. The transverse-electric (TE) waves are reflected by the metallic grating, while the TM waves are partially transmitted through the slits in the subwavelength region. Here, we assume the **X** and **Y** axes are perpendicular and parallel to the strips of the grating, respectively. The scattering matrix **S** determines electric field components for the TE or TM waves as

$$\begin{pmatrix} E^{b}_{\mathrm{I},p} \\ E^{f}_{\mathrm{II},p} \end{pmatrix} = \begin{pmatrix} S^{\sigma}_{11} & S^{\sigma}_{12} \\ S^{\sigma}_{21} & S^{\sigma}_{22} \end{pmatrix} \begin{pmatrix} E^{f}_{\mathrm{I},p} \\ E^{b}_{\mathrm{II},p} \end{pmatrix} = \begin{pmatrix} r & t \\ t & r \end{pmatrix} \begin{pmatrix} E^{f}_{\mathrm{I},p} \\ E^{b}_{\mathrm{II},p} \end{pmatrix} \quad (3)$$

where the superscripts f and b stand for "forwards" and "backwards," respectively. The grating is sandwiched by two dielectric materials I and II, respectively, and the corresponding field components along p = **X** or **Y** axis are labeled with the subscripts I or II. And r and t are zero-order reflection and transmission coefficients, respectively. For polarization σ = TE, the electric field is along **Y** axis, we have $r = -1$ and $t = 0$ in Equation (3); while for polarization σ = TM, the electric field is along **X** axis, we derive the **S** matrix using the FDTD method. Besides, if the electromagnetic waves incident on the grating with rotation angle θ, the **S** matrix can be achieved by rotation operation as

$$\mathbf{S}' = \begin{pmatrix} \mathbf{T}(\theta) & 0 \\ 0 & \mathbf{T}(\theta) \end{pmatrix}^{-1} \mathbf{S} \begin{pmatrix} \mathbf{T}(\theta) & 0 \\ 0 & \mathbf{T}(\theta) \end{pmatrix} \quad (4)$$

where $\mathbf{T}(\theta) = \begin{pmatrix} \cos(\theta) & -\sin(\theta) \\ \sin(\theta) & \cos(\theta) \end{pmatrix}$ is the rotation operator.

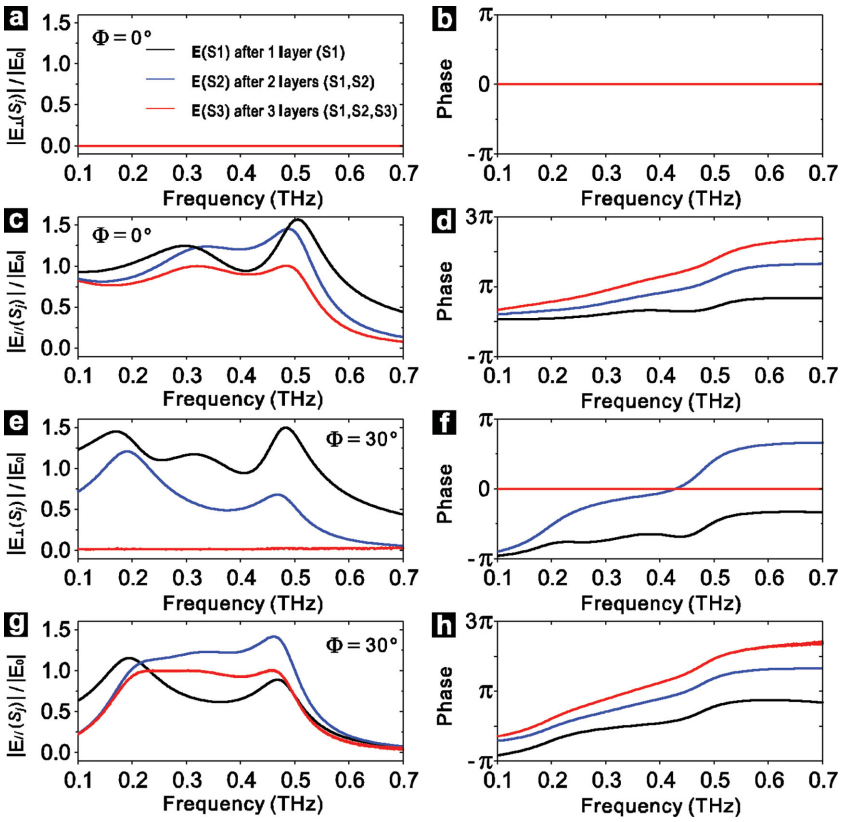

Figure 3. Frequency-dependent electric fields at three different spatial locations in the three-grating polarization rotator. The calculated electric fields, i.e., $\mathbf{E}(S_j)$ with S_j = S1, S2, and S3, after the THz waves immediately pass through the first grating layer S1 (black), second grating layer S2 (blue), and third grating layer S3 (red), respectively. Denote $\mathbf{E}_{||}(S_j)$ and $\mathbf{E}_{\perp}(S_j)$ as the field components parallel and perpendicular to the designed polarization direction, respectively. In the rotator with rotation angle $\Phi = 0°$: a) intensity and b) phase of $\mathbf{E}_{\perp}(S_j)$; c) intensity; and d) phase of $\mathbf{E}_{||}(S_j)$. While in the rotator with $\Phi = 30°$: e) intensity and f) phase of $\mathbf{E}_{\perp}(S_j)$; and g) intensity and h) phase of $\mathbf{E}_{||}(S_j)$. The incident wave is TM-polarized to the surface of the first grating S1. $d_1 = 300$ μm, $w_1 = 120$ μm, $d_2 = 380$ μm, $w_2 = 120$ μm, $h = 50$ μm, and $s = 60$ μm.

The polarized waves transmitting through the three-layer gratings can be described by the **S** matrix for the entire system using the iteration rule. Based on the scattering matrices, we have obtained the theoretical $T_{||}(\Phi)$ curves of the above broadband linear polarization rotator (see Figure S5 in the Supporting Information) for Φ = 0°, 30°, 45°, and 60°, respectively. These analytical results are consistent with the FDTD numerical calculations and the experimentally measured $T_{||}(\Phi)$ curves.

In order to understand how the polarization is rotated by the three-layer gratings, we can further calculate the electromagnetic fields inside the gratings using the transfer matrix **T**, which can be derived from the **S** matrix as

$$\mathbf{T} = \begin{pmatrix} \mathbf{S}_{21} - \mathbf{S}_{22}(\mathbf{S}_{12})^{-1}\mathbf{S}_{11} & \mathbf{S}_{22}(\mathbf{S}_{12})^{-1} \\ -(\mathbf{S}_{12})^{-1}\mathbf{S}_{11} & (\mathbf{S}_{12})^{-1} \end{pmatrix} \quad (5)$$

where $\mathbf{S}_{11}$, $\mathbf{S}_{12}$, $\mathbf{S}_{21}$, and $\mathbf{S}_{22}$ are the 2 × 2 block matrices of $\mathbf{S} = \begin{pmatrix} \mathbf{S}_{11} & \mathbf{S}_{12} \\ \mathbf{S}_{21} & \mathbf{S}_{22} \end{pmatrix}$. **Figure 3** shows the frequency-dependent electric fields at three different spatial locations in a rotator. $\mathbf{E}(S_j)$ with S_j = S1, S2, and S3, respectively, stands for the electric field

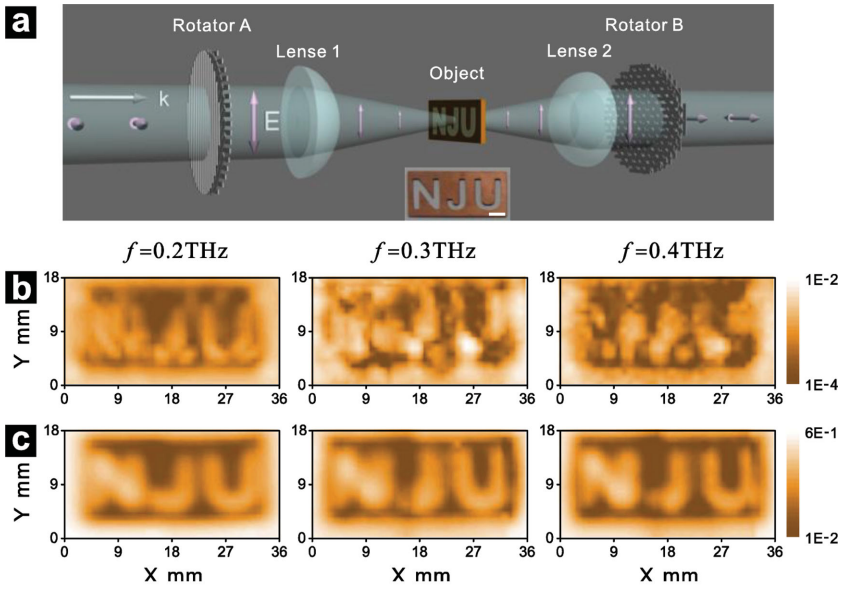

Figure 4. Visualization of polarization rotation by THz imaging. a) Schematic of the THz imaging system. Rotators A and B are two identical linear polarization rotators placed with mirror symmetry, both with $\Phi = 90°$, $d_1 = 300$ μm, $w_1 = 120$ μm, $d_2 = 380$ μm, $w_2 = 120$ μm, $h = 50$ μm, and $s = 60$ μm. The inset is a photograph of the imaging object with the scale bar being 5 mm long. Detected images of the object for frequencies $f = 0.2$, 0.3, and 0.4 THz under the conditions of b) with Rotator A but without Rotator B and c) with both Rotators A and B. Each 2D image consists of 73 × 145 pixels. The color bars show the transmission intensity levels on the logarithmic scale, with brighter areas corresponding to higher transmission.

immediately after the THz waves pass through the first grating layer S1, the second grating layer S2, and the third grating layer S3. Here, we use $\mathbf{E}_{||}(S_j)$ and $\mathbf{E}_{\perp}(S_j)$ representing the field components parallel and perpendicular to the designed polarization direction, respectively. In the tri-grating rotator with rotation angle $\Phi = 0°$, $\mathbf{E}_{\perp}(S_j)$ vanishes, while $|\mathbf{E}_{||}(S_j)|$ has high intensities. The phases of $\mathbf{E}_{||}(S_j)$ does not change abruptly, indicating that there are no resonances in the structure. While in the tri-grating rotator with $\Phi = 30°$ (similar to other cases with $\Phi \neq 0°$), $\mathbf{E}_{\perp}(S3)$ tends to vanish, yet $\mathbf{E}_{||}(S3)$ exists when the waves pass through the whole device. This feature determines the overall transmission and illustrates the polarization conversion of the THz wave. It is noteworthy that the ratio $|\mathbf{E}_{||}(S3)|/|\mathbf{E}_0|$ approaches 100% within broad bandwidth, indicating that a nearly perfect polarization conversion efficiency $\eta \cong 100\%$ has been realized. Note that both $|\mathbf{E}(S1)|$ and $|\mathbf{E}(S2)|$ may become larger than $|\mathbf{E}_0|$ at some frequencies when the waves travel between the first and the third gratings (as shown in Figure 3), which represents a typical feature for optical constructive interference.[33] In whole process, energy conservation sustains, yet the energy density is unevenly distributed in space.

Actually, when the TM waves pass through the first grating, they are split into both TE and TM waves to the second grating. The TE waves travel back and forth between the first and the second gratings; for TM waves, a part is reflected and the rest passes through the second grating. Similar processes happen in-between the second and the third gratings. Those transmission and reflection processes repeat, the constructive interference of multiple TM waves transmitting through the third grating (S3) lead to nearly perfect polarization conversion. Therefore these three gratings are strongly correlated in the device, acting as a three-dimensional (3D) structure. In this 3D tri-grating structure, the TM and TE waves are interswitchable, and multiwave interference occurs, eventually perfect polarization conversion is realized at optimal geometry. We should point out that the efficiency of polarization conversion in this tri-grating structure strongly depends on the thickness and the period of gratings, as well as the separations among three gratings (see the Supporting Information for details). In addition, because the thickness of the device is subwavelength, the optical phases for different frequencies do not change too much within this limited space. It follows that the polarization conversion of this device is a broadband effect. By decreasing the thickness of gratings or shrinking the separation of gratings in the device, the bandwidth for high polarization conversion can be enlarged yet the band shifts to the higher frequency region (see Figures S6–S8 in Supporting Information). Therefore, our theoretical analysis reveals that this polarization rotation originates from multi wave interference at THz regime in the three-layer grating structure.

The nearly perfect broadband polarization conversion can also be directly visualized through THz imaging. As schematically shown in **Figure 4**a, in our imaging experiments the TM-polarized polychromatic THz pulses are transmitted through Rotator A, and then focused onto the imaging objects. The transmitted signals through the objects are detected directly (without Rotator B) or detected after transmitted through Rotator B. Here, Rotators A and B are two linear polarization rotators placed with mirror symmetry, both with $\Phi = 90°$, $d_1 = 300$ μm, $w_1 = 120$ μm, $d_2 = 380$ μm, $w_2 = 120$ μm, $h = 50$ μm, and $s = 60$ μm. The polyethylene focusing lenses have focal lengths of 5.0 cm, and the objects are mounted on a computer-controlled **X-Y** stage, allowing continuous scanning via a focused beam for two-dimensional (2D) image generation at selected frequencies. The imaging objects are three-letter patterns, "N," "J," and "U," cut from a copper plate (see the inset of Figure 4a). Note that the copper plate is completely opaque to THz waves. The scanning step here is 1 mm, and we perform intermediate interpolation twice between two neighboring data sets to smooth the images.

First, we put only Rotator A in the system (without Rotator B) and image the objects at frequencies $f = 0.2$, 0.3, and 0.4 THz, respectively. As shown in Figure 4b, no clear pattern is formed, and overall the detected intensity is very low. However, if we move in Rotator B in the system (as schematically shown in Figure 4a), the images detected at $f = 0.2$, 0.3, and 0.4 THz clearly show the pattern "NJU" in Figure 4c, where the image contrast can reach about 60:1, and the average transmission intensity becomes very high. The fuzzy boundaries of the images are due to the diffraction limit as the incident

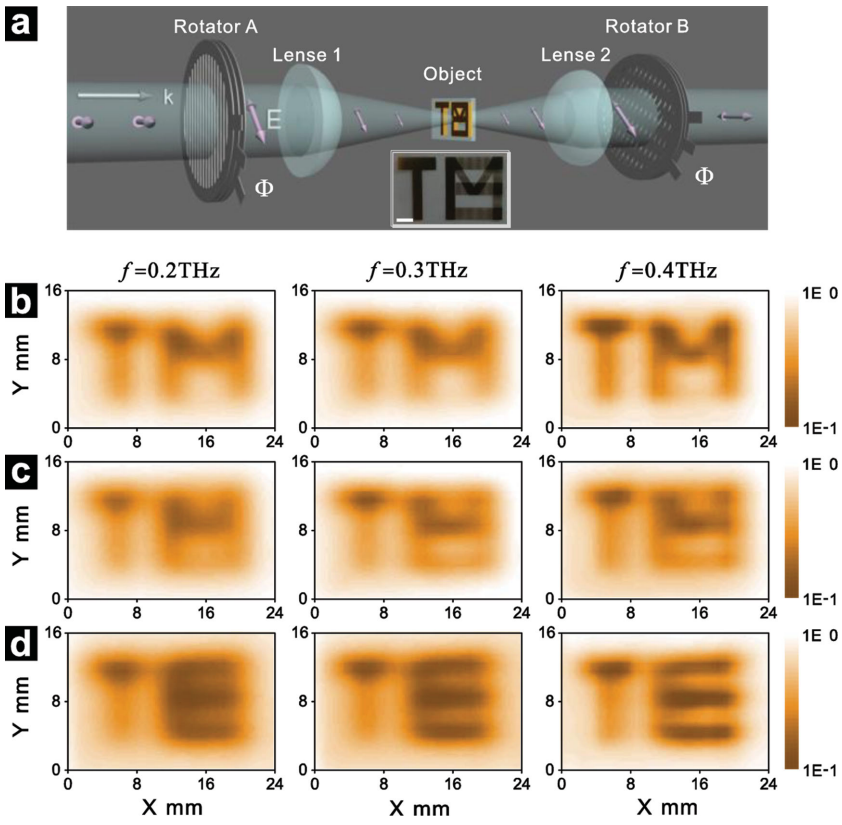

Figure 5. THz imaging of a polarization-sensitive sample with the mechanical tunability of the polarization rotators. a) Schematic of the THz imaging system. Rotators A and B are the same as those in Figure 4a. The inset is a photograph of the imaging object and the scale bar is 2.5 mm. Detected images of the object sample for frequencies $f = 0.2$, 0.3, and 0.4 THz under the polarization rotation angles of b) $\Phi = 0°$; c) $\Phi = 45°$; and d) $\Phi = 90°$. Each 2D image consists of 65×97 pixels.

wavelength is comparable to the boundary width of the sample patterns. The imaging resolution improves with increasing f. Actually in the experiments, the polarization of the incident waves were rotated 90° by Rotator A, then the same polarization was kept after the waves passing the imaging objects ("NJU"). Note that the detector can only collect the signals with the same polarization of incident waves, thus the signals with orthogonal polarization can not be detected if Rotator B does not exist in the system. But once we put Rotator B into the system, the polarization of the transmitted wave was further rotated 90° by Rotator B, turning to be parallel polarization to incident waves, thus the transmitted signals were received by the detector. These results clearly demonstrate that Rotators A and B can indeed effectively rotate the linear polarization in the desired way.

Mechanical tuning is an effective way to achieve active devices.[34–39] In our case, the broadband linear polarization rotator is mechanically tunable, which can also be demonstrated through THz imaging of a polarization-sensitive sample. As schematically shown in **Figure 5**a, the linear polarization states of the THz waves can be arbitrarily changed between the two polarization rotators. Here, we use a polarization-sensitive imaging sample, which combines the "TM" and "TE" patterns using two orthogonal gratings to distinguish the differences between the two patterns (see the inset of Figure 5a and its magnification in Figure S1 of the Supporting Information). This sample is a 50-nm-thick gold layer on a polyethylene terephthalate substrate constructed with lithography.

When both Rotators A and B are mechanically rotated to $\Phi = 0°$, the polarization states of the THz waves between two rotators are not changed, thus the detected images at $f =$ 0.2, 0.3, and 0.4 THz clearly show the "TM" pattern in Figure 5b. When the two rotators are set to $\Phi = 45°$, we obtain the overlapped "TM" and "TE" patterns in Figure 5c. As expected, when A and B are mechanically set to $\Phi = 90°$, the polarization states of the THz waves become orthogonal states compared with the waves outside two rotators, thus clear "TE" patterns are recorded in Figure 5d (Note that in all the three cases, the sample is fixed). The image contrast is about 10:1 in Figure 5 (the dark images under bright background), which is reasonably lower than that in Figure 4 (the bright images under dark background). Based on these results on the polarization-sensitive sample, therefore, we have verified the tri-grating rotator's capability of free polarization rotation to any direction.

In conclusion, we have demonstrated a linear polarization rotator that is a three-layer metallic grating structure for manipulating the polarization of broadband THz waves. By mechanical rotations of the composite grating layers, this freely tunable device can rotate the polarization of a linearly polarized THz wave to any desired direction with high conversion efficiency. It is a subwavelength device that has a thickness of less than one quarter of the central wavelength in the working band. The excellent performance of this device is experimentally shown by both THz transmission measurements and direct THz imaging. The polarization rotation effect originates from multiwave interference in the three-layer grating structure. This low-cost, thin, high-efficiency, and freely tunable broadband THz device may have potential applications in various areas, such as material analysis, wireless communication, and THz imaging.

Acknowledgements

This work was supported by the Ministry of Science and Technology of China (Grant No. 2012CB921502), the National Natural Science Foundation of China (Grant Nos. 11034005, 61475070, 11474157, 11321063, and 91321312), and partially by the China Postdoctoral Science Foundation (Grant No. 2014M551548), and X.R.H. was supported by the US Department of Energy, Office of Science, Office of Basic Energy Sciences, under Contract No. DE-AC02–06CH11357.

Received: October 31, 2014
Revised: November 21, 2014
Published online: December 28, 2014

[1] P. H. Siegel, *IEEE Trans. Microwave Theory Tech.* **2002**, *50*, 910.
[2] B. Ferguson, X. C. Zhang, *Nat. Mater.* **2002**, *1*, 26.
[3] M. Tonouchi, *Nat. Photonics* **2007**, *1*, 97.
[4] A. V. Rogacheva, V. A. Fedotov, A. S. Schwanecke, N. I. Zheludev, *Phys. Rev. Lett.* **2006**, *97*, 177401.
[5] J. Hao, Y. Yuan, L. Ran, T. Jiang, J. A. Kong, C. T. Chan, L. Zhou, *Phys. Rev. Lett.* **2007**, *99*, 063908.
[6] N. Kanda, K. Konishi, M. Kuwata-Gonokami, *Opt. Express* **2007**, *15*, 11117.
[7] J. K. Gansel, M. Thiel, M. S. Rill, M. Decker, K. Bade, V. Saile, G. von Freymann, S. Linden, M. Wegener, *Science* **2009**, *325*, 1513.
[8] I. Yamada, K. Takano, M. Hangyo, M. Saito, W. Watanabe, *Opt. Lett.* **2009**, *34*, 274.
[9] C. Wu, H. Q. Li, X. Yu, F. Li, H. Chen, C. T. Chan, *Phys. Rev. Lett.* **2011**, *107*, 177401.
[10] Y. Zhao, M. A. Belkin, A. Alù, *Nat. Commun.* **2012**, *3*, 870.
[11] L. Cong, W. Cao, Z. Tian, J. Gu, J. Han, W. Zhang, *New J. Phys.* **2012**, *14*, 115013.
[12] L. Ren, C. L. Pint, T. Arikawa, K. Takeya, I. Kawayama, M. Tonouchi, R. H. Hauge, J. Kono, *Nano Lett.* **2012**, *12*, 787.
[13] N. K. Grady, J. E. Heyes, D. R. Chowdhury, Y. Zeng, M. T. Reiten, A. K. Azad, A. J. Taylor, D. A. R. Dalvit, H.-T. Chen, *Science* **2013**, *340*, 1304.
[14] L. Cong, W. Cao, X. Zhang, Z. Tian, J. Gu, R. Singh, J. Han, W. Zhang, *Appl. Phys. Lett.* **2013**, *103*, 171107.
[15] S. C. Jiang, X. Xiong, P. Sarriugarte, S. W. Jiang, X. B. Yin, Y. Wang, R. W. Peng, D. Wu, R. Hillenbrand, X. Zhang, Mu Wang, *Phys. Rev. B* **2013**, *88*, 161104(R).
[16] S. Wu, Z. Zhang, Y. Zhang, K. Y. Zhang, L. Zhou, X. J. Zhang, Y. Y. Zhu, *Phys. Rev. Lett.* **2013**, *110*, 207401.
[17] S. C. Jiang, X. Xiong, Y. S. Hu, Y. H. Hu, G. B Ma, R. W. Peng, C. Sun, Mu Wang, *Phys. Rev. X* **2014**, *4*, 021026.
[18] T. T. Lv, Z. Zhu, J. H. Shi, C. Y. Guan, Z. P. Wang, T. J. Cui, *Opt. Lett.* **2014**, *39*, 3066.
[19] H.-T. Chen, W. J. Padilla, M. J. Cich, A. K. Azad, R. D. Averitt, A. J. Taylor, *Nat. Photonics* **2009**, *3*, 148.
[20] B. Gholipour, J. Zhang, K. F. MacDonald, D. W. Hewak, N. I. Zheludev, *Adv. Mater.* **2013**, *25*, 3050.
[21] X. Zhang, Z. Tian, W. Yue, J. Gu, S. Zhang, J. Han, W. Zhang, *Adv. Mater.* **2013**, *25*, 4567.
[22] J. Neu, B. Krolla, O. Paul, B. Reinhard, R. Beigang, M. Rahm, *Opt. Express* **2010**, *18*, 27748.
[23] B. Scherger, C. Jördens, M. Koch, *Opt. Express* **2011**, *19*, 4528.
[24] D. Grischkowsky, S. Keiding, M. van Exter, C. Fattinger, *J. Opt. Soc. Am. B* **1990**, *7*, 2006.
[25] D. Grischkowsky, S. Keiding, *Appl. Phys. Lett.* **1990**, *57*, 1055.
[26] T. Nose, S. Sato, K. Mizuno, J. Bae, T. Nozokido, *Appl. Opt.* **1997**, *36*, 6383.
[27] T.-R. Tsai, C.-Y. Chen, R.-P. Pan, C.-L. Pan, X.-C. Zhang, *IEEE Microwave Wireless Compon. Lett.* **2004**, *14*, 77.
[28] F. Rutz, T. Hasek, M. Koch, H. Richter, U. Ewert, *Appl. Phys. Lett.* **2006**, *89*, 221911.
[29] A. Taflove, S. C. Hagness, *Computational Electrodynamics: The Finite-Difference Time-Domain Method*, 3rd ed., Artech House, Norwood, **2005**.
[30] A. Figotin, I. Vitebsky, *Phys. Rev. E* **2001**, *63*, 066609.
[31] A. Figotin, I. Vitebskiy, *Phys. Rev. B* **2003**, *67*, 165210.
[32] Y. Zhou, Y. Q. Dong, R. H. Fan, Q. Hu, R. W. Peng, Mu Wang, *Appl. Phys. Lett.* **2014**, *105*, 041114.
[33] M. Born, E. Wolf, *Principles of Optics*, 7th ed., Cambridge University Press, Cambridge, **1999**.
[34] Y. Zhao, S. Bai, D. Dumont, T. V. Galstian, *Adv. Mater.* **2002**, *14*, 512.
[35] Y.-F. Chen, Y. F. Mei, R. Kaltofen, J. I. Mönch, J. Schumann, J. Freudenberger, H. J. Klauß, O. G. Schmidt, *Adv. Mater.* **2008**, *20*, 3224.
[36] J. H. So, J. Thelen, A. Qusba, G. J. Hayes, G. Lazzi, M. D. Dickey, *Adv. Funct. Mater.* **2009**, *19*, 3632.
[37] R. H. Fan, R. W. Peng, X. R. Huang, J. Li, Y. Liu, Q. Hu, Mu Wang, X. Zhang, *Adv. Mater.* **2012**, *24*, 1980.
[38] J. Li, C. M. Shah, W. Withayachumnankul, B. S.-Y. Ung, A. Mitchell, S. Sriram, M. Bhaskaran, S. Chang, D. Abbott, *Appl. Phys. Lett.* **2013**, *102*, 121101.
[39] R. H. Fan, J. Li, R. W. Peng, X. R. Huang, D. X. Qi, D. H. Xu, X. P. Ren, Mu Wang, *Appl. Phys. Lett.* **2013**, *102*, 171904.